PHYSICAL REVIEW MATERIALS **7**, 034001 (2023)

Editors' Suggestion

Stacking domain morphology in epitaxial graphene on silicon carbide

Tobias A. de Jong,[1,*] Luuk Visser,[1] Johannes Jobst,[1] Ruud M. Tromp,[2,1] and Sense Jan van der Molen[1,†]

[1]*Huygens-Kamerlingh Onnes Laboratorium, Leiden Institute of Physics, Leiden University, Niels Bohrweg 2, P.O. Box 9504, NL-2300 RA Leiden, The Netherlands*

[2]*IBM Thomas J. Watson Research Center, 1101 Kitchawan Road, P.O. Box 218, Yorktown Heights, New York 10598, USA*

(Received 29 July 2022; revised 30 November 2022; accepted 23 December 2022; published 17 March 2023)

Terrace-sized, single-orientation graphene can be grown on top of a carbon buffer layer on silicon carbide by thermal decomposition. Despite its homogeneous appearance, a surprisingly large variation in electron transport properties is observed. Here, we employ aberration-corrected low-energy electron microscopy to study a possible cause of this variability. We characterize the morphology of stacking domains between the graphene and the buffer layer of three different high-quality samples to capture the range of possible behavior. Similar to the case of twisted bilayer graphene, the lattice mismatch between the graphene layer and the buffer layer at the growth temperature causes a moiré pattern with domain boundaries between AB and BA stackings. We analyze this moiré pattern to characterize the relative strain and to count the number of edge dislocations. Furthermore, we show that epitaxial graphene on silicon carbide in general is close to a phase transition, causing intrinsic disorder in the form of the coexistence of anisotropic stripe domains and isotropic trigonal domains. Using adaptive geometric phase analysis, we determine the precise relative strain variation caused by these domains in different samples. We observe that the step edges of the SiC substrate influence the orientation of the domains and we discuss which aspects of the growth process influence these effects by comparing samples from different sources.

DOI: 10.1103/PhysRevMaterials.7.034001

I. INTRODUCTION

Epitaxial graphene on silicon carbide can be grown on the wafer scale by thermal decomposition, on both doped and insulating SiC substrates. As silicon has a lower sublimation point than carbon, by heating an atomically flat surface of SiC to 1200 °C or higher, the silicon sublimates, while the carbon stays behind [1,2]. The first layer of carbon is hexagonal, but still covalently bonded to the substrate. This means this so-called buffer layer lacks full sp^2 hybridization, preventing the π bands from forming, giving it a more insulating character [3,4]. The subsequent layer(s) do exhibit full sp^2 hybridization and are therefore only bonded to the other layer(s) by van der Waals forces. Growing the graphene at higher temperatures or keeping it hot for longer causes more silicon to sublimate and extra layers to form between the buffer layer and the top graphene layer [5,6]. Although growth on the carbon face of the SiC is possible, here we focus on the more homogeneous graphene growth on the Si face. To create more regular layers, a gas back pressure of silane or, more commonly, argon of up to one bar can be supplied. This achieves more uniform growth at lower speeds and higher temperatures [7,8]. Additionally, extra carbon can be provided by depositing carbon in advance [9,10]. Optimization of these growth procedures has led to very homogeneous monolayer graphene on SiC samples, but a surprisingly large variation of electron transport properties remains in these samples [11].

The graphene lies on a buffer layer covalently bonded to the SiC and forms a $(6\sqrt{3}\times 6\sqrt{3})R30^\circ$ reconstruction with the underlying SiC lattice [2,12]. However, as the ratio of the lattice constants of graphene and SiC does not perfectly adhere to the ratio given by the reconstruction and both materials exhibit different thermal expansion rates, stacking domain boundaries occur to resolve the additional lattice mismatch. The resulting lattice mismatch is nevertheless small and notably no observation of it has been reported in low-energy electron diffraction. Such stacking domains have been observed before in real space, including using dark-field low-energy electron microscopy (LEEM), thermoelectric imaging, and scanning tunneling microscopy [13–16]. In bilayer graphene, the boundaries of such stacking domains host topological edge states [17–20]. Although the buffer layer has obviously different electronic properties than graphene, this suggests that these domains should have an influence on the electronic transport properties, at the very least in the case of intercalated, quasifreestanding bilayer graphene, where the buffer layer has been "upgraded" to a true graphene layer [3].

Here, we study these stacking domain boundaries in high-quality epitaxial graphene obtained via three different growth processes. We directly image the domain boundaries in these samples using bright-field low-energy electron microscopy at an electron landing energy $E_0 \approx 40$ eV [21]. By employing stitching of high-resolution, aberration-corrected low-energy electron microscopy (AC-LEEM) data as described in Ref. [22], we obtain a field of view exceeding $10 \times 10\ \mu\text{m}^2$, while retaining a high resolution of at least 2.2 nm/pixel to characterize the stacking domain boundaries, enabling the gathering of statistics and the extraction

---

[*] jongt@physics.leidenuniv.nl

[†] molen@physics.leidenuniv.nl

of properties of the graphene itself. By repeating this for three different growth processes, we capture a wide gamut of possible morphologies in this class of samples, showing both the universal aspects and what can differ between samples.

The three samples imaged in this way are the following. First, *sample A*, which was grown by the Weber group at the University of Erlangen-Nürnberg using an early prototype of a variation on polymer-assisted growth, where a layer of carbon is sputtered onto the SiC before growth. This sample is grown with an argon back pressure to enable uniform growth and hydrogen intercalated to create a quasifreestanding bilayer graphene [23]. Second, *sample B* is a commercially bought sample from the company Graphensic, which bases its growth process on the work of the group of Professor Yakimova at Linköping University [24]. Finally, *sample C* was grown at the PTB in Braunschweig using polymer-assisted sublimation growth in argon back pressure [9,10].

In the next section, the full datasets are shown and the visible features in the images are described qualitatively. Then we will use adaptive geometric phase analysis (GPA) to quantitatively analyze the domain sizes and relate these to the strain in the layers. In Secs. IV and V, we will take a closer look at two peculiar features, i.e., spiral domain walls and edge dislocations, before we will interpret the results and draw conclusions about strain and local variation in these materials.

The PYTHON code used to generate the figures in this work is available as open source in Ref. [25] and the underlying data are available in Ref. [26].

II. QUALITATIVE DESCRIPTION OF SAMPLE FEATURES

Before analysis, each of the full datasets is normalized by dividing by a smoothed version of itself with a width of $\sigma = 50$ pixels, where for samples B and C the bilayer areas are normalized separately.

For sample A, an area of 305 μm^2 is imaged at a resolution of 2.2 nm/pixel with an average total integration time of 194.7 s (for each pixel). For sample B, an area of 111 μm^2, of which 7.1% is bilayer, is imaged at 1.4 nm/pixel with an average total integration time of 103.8 s. For sample C, an area of 112 μm^2, of which 3.5% is bilayer, is imaged at a resolution of 2.2 nm/pixel with an average total integration time of 16.6 s.

For all three samples, terrace step edges of the SiC substrate are visible, running roughly horizontal. On all samples, some conglomerated carbohydrate adsorbates are visible as black spots, sticking to these substrate step edges and some other defects. Sample A shows more adsorbates than the other samples, but this is not due to the growth procedure, but due to sample handling and imaging conditions. This sample also shows additional defect lines running roughly vertical. Two examples are indicated with red arrows in Fig. 1(a). As they terminate in points (indicated with red circles) and cross substrate steps, they seem unlikely to be terrace edges. Instead, they are probably folds or residue from excess carbon from the experimental carbonated growth process.

All three samples show some bilayer areas, appearing bright in Figs. 1(b) and 1(c). For sample A, they appear dark [e.g., just above and below the center, indicated with orange arrows in Fig. 1(a)], due to the different value of the electron landing energy E_0 that is used and the hydrogen intercalation. Furthermore, both of the samples in Figs. 1(b) and 1(c) show terraces with a slightly different contrast, next to the lower bilayer area in Fig. 1(b) (indicated with a green arrow) and in several spots in Fig. 1(c), in particular in round spots in the center of the terraces (some examples are indicated with green arrows). This difference in intensity is due to the stacking order and termination of the underlying silicon carbide [27,28].

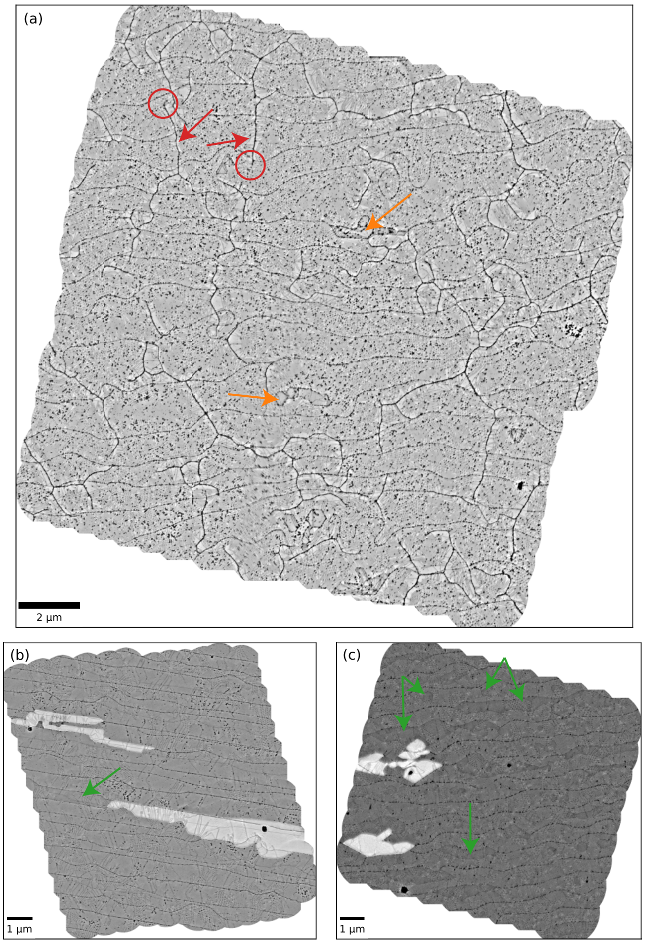

FIG. 1. Sample overviews. (a) Sample A, intercalated quasifreestanding graphene on SiC, grown using an experimental carbonated growth from Weber's group in Erlangen-Nürnberg [23], imaged using BF-LEEM at $E_0 = 40$ eV. (b) Sample B, commercially bought graphene on 4H-SiC from Graphensic based on the Linköping growth technique, imaged at $E_0 = 37$ eV. (c) Sample C, polymer-assisted sublimation growth on 6H-SiC sample grown at PTB Braunschweig, imaged at $E_0 = 36$ eV. All full areas are normalized by dividing by a Gaussian smoothed version of the image (with width $\sigma = 50$ pixels) to eliminate global brightness variations, treating (brighter) bilayer areas separately for (b) and (c). Details about the indicated features are given in the main text.

Of the three samples, sample A is the most irregular. In addition to the aforementioned vertically running defect lines, the SiC substrate step edges are wavier than in the other two samples, although further apart, due to a step bunching procedure applied in the process before graphene growth, as described in the methods section of Ref. [13]. In Fig. 2, some full-resolution detail images showcase the domain boundary

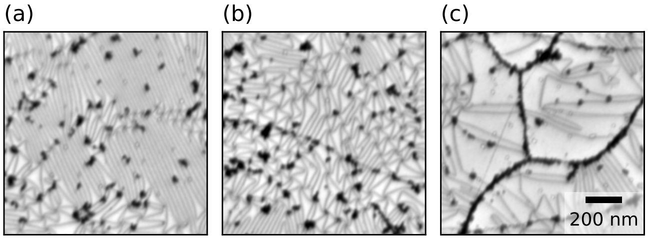

FIG. 2. Details in sample A. (a) Striped stacking domains. (b) Chaotic triangular stacking domains. Domain boundaries cross the horizontal step edge in this field of view. (c) Along the vertical dark features on this sample, significantly larger domains occur. All panels have the same scale.

morphology. The domain shapes are irregular. Stripe domains [Fig. 2(a)] occur in roughly three directions. Triangular domains occur as well, but are irregularly shaped, not forming larger regular grids [Fig. 2(b)]. Remarkably, around the defect lines, domains are significantly larger and irregular [Fig. 2(c)], suggesting they are folds out of plane which absorb some of the lattice mismatch.

Sample B is much more regular. In Figs. 3(a) and 3(b), it is visible that both relatively regular triangular domains and very dense stripe domains occur [29,30]. Although these stripe domains again occur in three directions, they occur parallel to the substrate step edges in the vast majority of the cases. Details of the bilayer-on-buffer-layer areas are shown in Figs. 3(c) and 3(d). Stripe domain boundaries occur between the buffer layer and the lower graphene layer, with the domain boundaries "twinning," i.e., forming pairs closer together, due to the energy mismatch between ABC and ABA stacked graphene [31–33]. Domain boundaries between the top two graphene layers also occur, distinguishable by a much higher contrast than those lower down, as expected [21]. However, they seem largely irregular, which matches earlier observations that those domain boundaries are caused by nucleation instead of strain [13–15]. However, in some areas where triangular domains border the bilayer, e.g., in Fig. 3(d), it seems that the domain boundaries in the monolayer on buffer layer connect to domain boundaries in the bilayer on buffer layer on both levels, i.e., alternating between the buffer layer and the bottom graphene layer and between the two graphene layers.

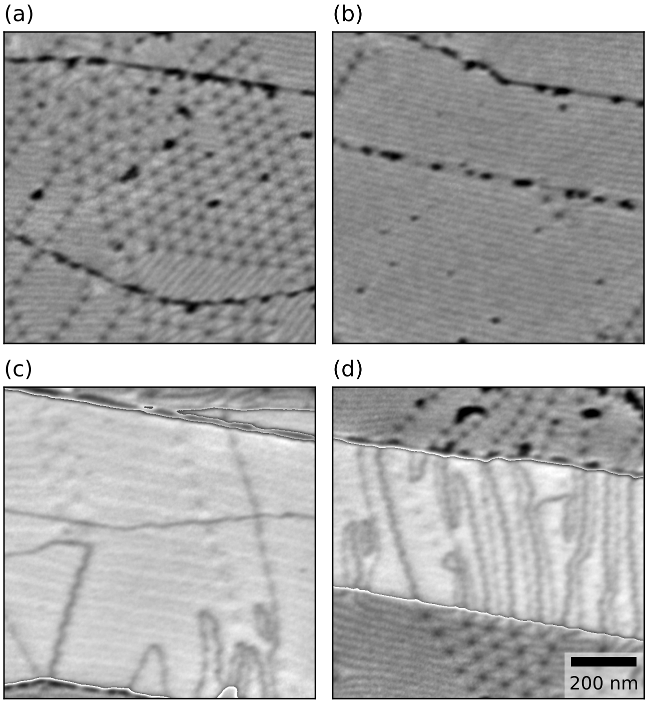

FIG. 3. Details in sample B. (a) More regular triangular stacking domains. (b) Very large and regular striped domains with high stripe density. (c) Domains in the bilayer region: Twinned stripe domains between the buffer layer and the lower graphene layer (faint horizontal lines) and irregular domains between the two graphene layers. (d) Relation between triangular domains in the monolayer and domain boundaries in the bilayer area. All panels have the same scale.

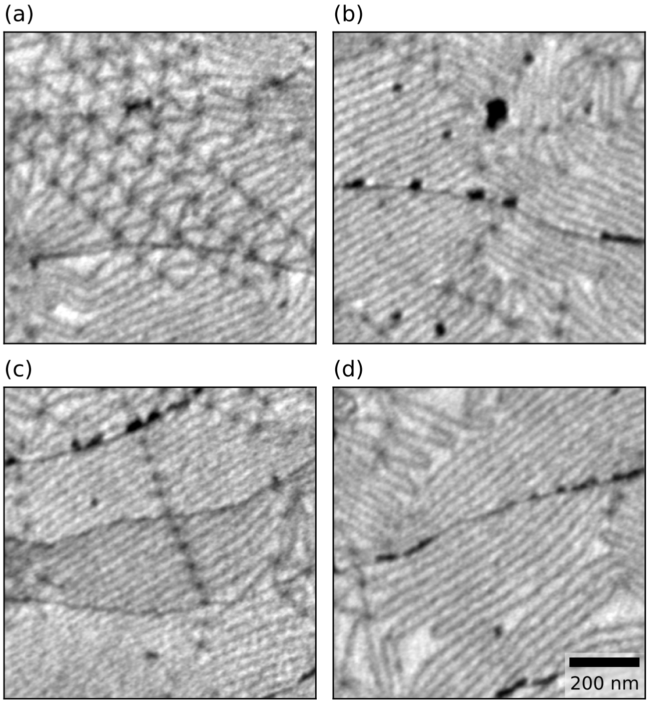

FIG. 4. Details in sample C. (a) Large triangular domains. (b) Stripe domains in two distinct directions. (c) Stripe domains with a node line crossing across substrate step edges. (d) Low-density stripes and disorder. All panels have the same scale.

For sample C, details are shown in Fig. 4. Some triangular domains occur, but a larger part is covered by stripe domains in three directions. Both the triangles and stripe widths vary, but generally are significantly larger than in sample B. Domain boundaries and even strings of AA nodes between stripe domains [Fig. 4(c), also occurring on sample B] seem to cross substrate step edges unperturbed. Finally, like in sample A, irregular domain shapes are quite common and will be explored in Sec. V. But first, in the next section, we will apply geometric phase analysis (GPA) to quantify the domain morphology and leverage the large size of the imaged areas to obtain some statistics.

III. STRIPE DOMAINS IN EPITAXIAL GRAPHENE

From the morphology of the domains as shown in the previous section, it was already clear that the graphene on SiC samples is less homogeneous than widely believed. Although strain in graphene on SiC and even nonhomogeneity of the strain have been studied extensively using, e.g., Raman spectroscopy [34–36], the mere existence of domain boundaries which concentrate the strain means that extra care should be taken in interpreting these results, as these techniques average over relatively large areas. In this section, we will extract more quantitative information from the stacking domains and use the relation between the stacking domains and the atomic lattice to quantify strain and disorder on the atomic level.

Assuming the amount of carbon atoms in the graphene layer is fixed after the growth stops, the average size of the domains is determined by the remaining mismatch between graphene and the $6\sqrt{3}$ reconstruction of the buffer layer on the SiC at the growth temperature [36]. The remaining mismatch between the lattice constants is given by

$$\epsilon = 1 - \frac{13a_{\mathrm{G}}}{6\sqrt{3}a_{\mathrm{SiC}}}.$$

This mismatch corresponds to a relative isotropic elongation of the buffer layer with respect to the graphene layer. Because this mismatch is relatively small (otherwise the reconstruction would not be able to form), accurate values of the relevant lattice parameters and their temperature dependence are needed to calculate the expected domain size. To obtain an estimate, we use the same values as used in Ref. [37]: $a_{\mathrm{SiC}} = 0.3096$ nm and $a_{\mathrm{G}} = 0.2458$ nm at $T \approx 1200\,^{\circ}\mathrm{C}$. This corresponds to a remaining lattice mismatch of $\epsilon = 0.7\%$ (where graphene has the smaller lattice constant compared to the buffer layer). Note that given the thermal expansion coefficients, this number is strongly dependent on the growth temperature, decreasing by about 0.05% for a 100 K lower growth temperature. Finally, it is claimed that a shorter growth time can give a small carbon deficiency, effectively yielding a tensile strain in the graphene layer at the growth temperature [36,38].

The two-dimensional Frenkel-Kontorova (FK) model can be used to describe domain formation in bilayer graphene due to a combination of the interlayer interaction and the elastic forces within the layer. While for small lattice mismatch values, i.e., $\epsilon < \epsilon_{c0}$, the layers will remain fully commensurate, for $\epsilon > \epsilon_{c2}$, the interlayer interaction will play no large role and both layers will form an almost unperturbed moiré pattern. However, in the intermediate regime, the interactions will cause Bernal stacked domains to form, and the FK model can be used to calculate the resulting domain size and a corresponding resulting average relative elongation $\tilde{\epsilon}$. In this work, we will express the domain size in terms of the line spacing $1/k = a\frac{1+\tilde{\epsilon}}{\tilde{\epsilon}}$, as this value is equal to the positions of the corresponding peaks in Fourier transforms of real-space images.

The FK model predicts an extra phase transition as a function of ϵ if crossings of domain boundaries, i.e., AA sites, cost extra energy compared to a noncrossing domain boundary. It is beneficial to form parallel domain boundaries instead of a triangular domain pattern by elongating triangular domains along one direction to essentially infinite length in one direction [see Fig. 5(a)] [39]. Note that this even holds for samples under isotropic elongation, if the energy cost of the AA sites is high enough compared to the energy cost of domain boundaries. The maximum energy of the relative stacking in the domain boundary corresponds to a saddle point in the energy landscape and is therefore called SP stacking [40]. This phase transition is a discontinuous, symmetry-breaking one and thus a first-order phase transition. For bilayer graphene, the ratio between stacking energy costs of AA stacking and SP stacking is about 9. This corresponds to stripe domains forming if the relative elongation is above a lower critical value of $\epsilon_{c1} = 0.37\%$. Therefore, stripe domains can be expected in graphene on SiC samples (assuming the graphene-buffer layer interaction is close enough to the one of bilayer graphene, or intercalated samples). For samples created with short enough

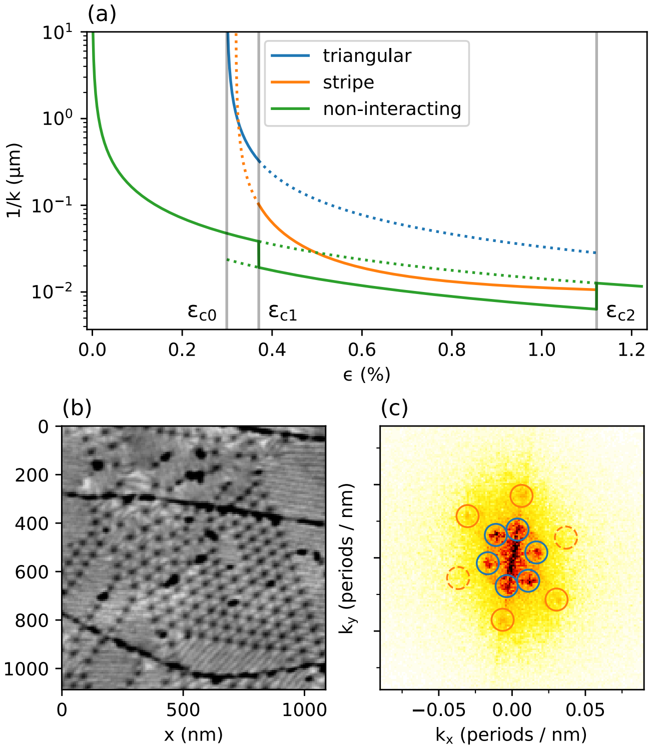

FIG. 5. Stripe and triangular phases. (a) Calculated phase diagram and period of the superstructure as a function of relative isotropic elongation in bilayer graphene as computed by Lebedeva and Popov for a barrier height of SP stacking of 1.61 meV/atom [39]. Phases are, from left to right, commensurate, triangular incommensurate, striped incommensurate, and again triangular commensurate. The solid line indicates the observable line spacing in the superstructure in the respective phases. Also indicated (in green) is the resulting periodicity of the respective phases for a lattice mismatch directly corresponding to the indicated strain, i.e., when contracting of the lattice due to interaction is not taken into account. (b) Small crop of sample B with both triangular domains and stripe domain in two directions. A straight and a curved step edge run horizontally through the image and are decorated with adsorbates appearing in black. (c) Center of the FFT of (b). Detected triangular domain spots are circled in blue. Four detected stripe domain spots are circled orange, and their difference used as the third reference vector is circled in dashed orange.

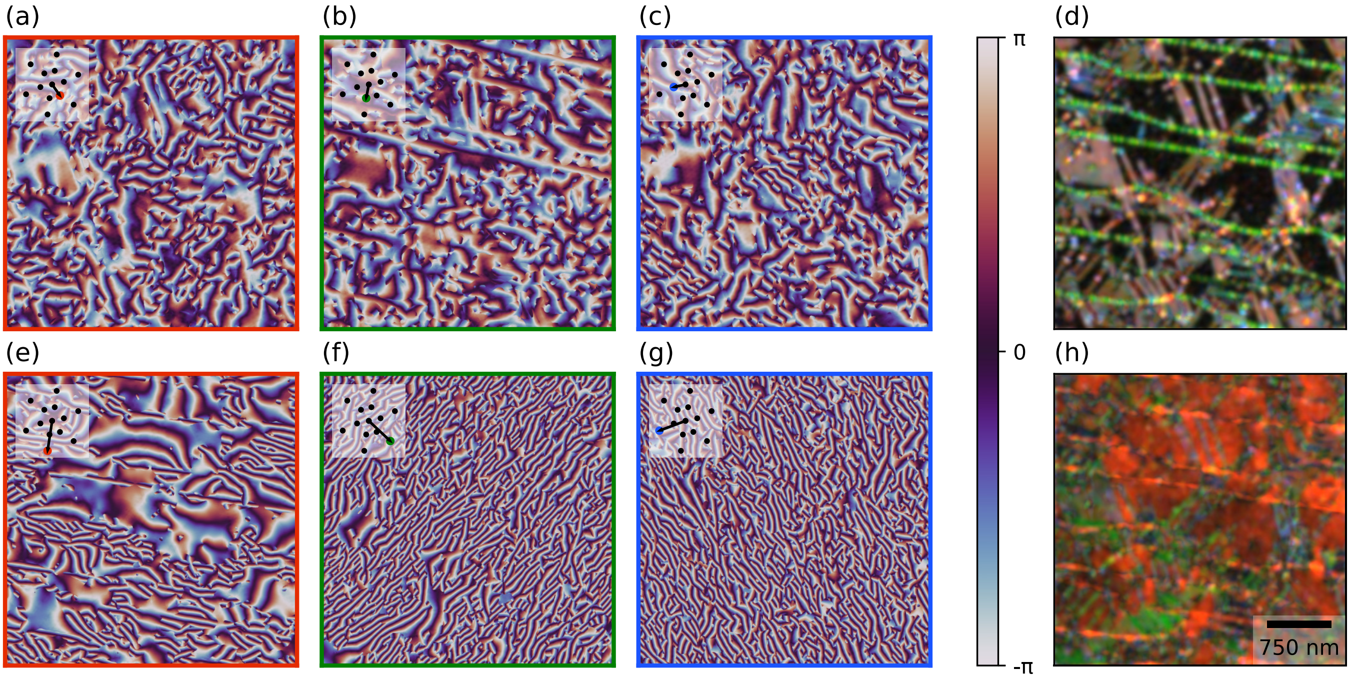

FIG. 6. GPA phase analysis on an area of sample B with both triangular and stripe domains. (a)–(c) GPA phases corresponding to triangular domains. The k vector used for each panel is indicated in its inset. (d) Normalized GPA amplitudes in RGB channels corresponding to the triangular domains. The substrate steps are visible as green lines. (e)–(g) GPA phases of stripe domains. (h) Similar to (d), but for the stripe phases. Red [i.e., (e)] corresponds to the dominantly present stripe phase.

growth times or at low enough temperature, a mixture of both parallel domain boundaries and triangular patterns can be expected. For stripe domains, the line spacing is given by $1/k = a\frac{1+\tilde{\epsilon}}{2\tilde{\epsilon}}$, as two domain boundaries form per unit cell.

Finally, note that as the sample cools after growth, the lattice mismatch between the graphene and the SiC reconstruction decreases (to 0.1% or less at room temperature), but the number of carbon atoms in the graphene layer is already roughly fixed and the graphene layer is pinned to the substrate by defects and step edges. This yields a total compressive strain on the graphene (which might be partially offset by a carbon deficiency tensile strain for short growth times), but the relative lattice mismatch is globally kept the same as both the layers are pinned to the substrate by defects.

Indeed, this is what we observe for the graphene on SiC samples, where the periodicity of the buffer layer is forced by the underlying SiC substrate, but the behavior of the graphene layer on top of that is governed by the van der Waals interaction and graphene's properties.

Note, however, that unlike on some metals [41,42], for these boundaries all the strain compensation happens in plane, i.e., no wrinkles form.

A. Geometric phase analysis analysis of strain

To characterize the stacking domains, we use (adaptive) geometric phase analysis (GPA), which uses a comparison to a perfect lattice to calculate the deformation of the domains [22,43]. Here, for each lattice vector (of the moiré lattice), the image is multiplied with the corresponding complex plane wave. After low-pass filtering in Fourier space, the result is a complex image, where the phase corresponds to the phase shift along the plane wave, and the magnitude is a local measure for how well the original image corresponds to (a shifted version of) the perfect lattice. Using the phases and magnitudes of several trial lattices, the deformation can be reconstructed. This approach is described in detail in Refs. [22,43]. In this way, we can extract local periodicities from the real-space images and calculate back to relative strain values.

The transition from triangular to striped domains causes the length of the corresponding k vector to double as one direction of domain boundaries aligns with a second to become parallel, thus doubling the frequency (with the third being pushed out). Therefore, stripe domains yield separate peaks at roughly double the frequency in the Fast Fourier Transform (FFT) of domain images compared to triangular domains, as highlighted in orange and blue, respectively, for sample B in Fig. 5. This relatively large separation in Fourier space between the triangular phase and the three striped phases means we can perform GPA for each separately and use this to distinguish them on a large scale and characterize each phase independently.

The GPA phases for the triangular phase of sample B are shown in Figs. 6(a)–6(c), and those for the stripe phase in Figs. 6(e)–6(g). For both the triangular and the stripe phases, the corresponding amplitudes are shown as red, green, and blue channels in Figs. 6(d) and 6(h), respectively.

The GPA phases only contain relevant information in the areas where the corresponding (stacking domain) phase occurs, as indicated by a high amplitude, and corresponding to a slowly varying GPA phase in real space.

By comparing the GPA amplitudes, we create a mask dividing the sample into stripe domains and triangular domains. For

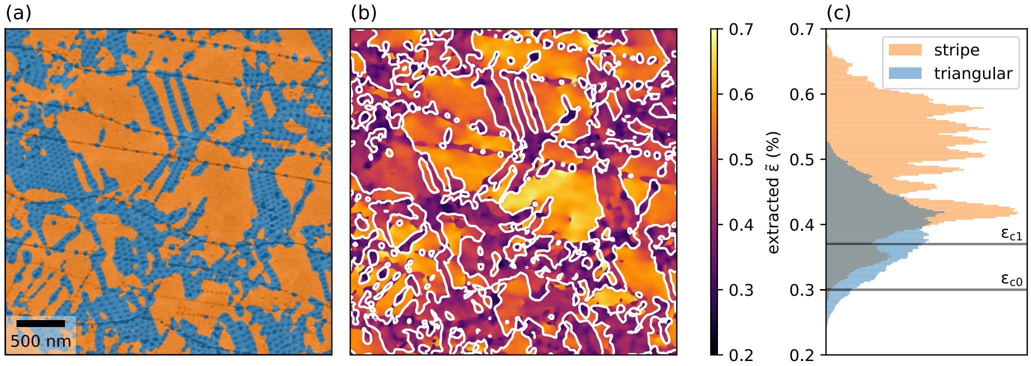

FIG. 7. (a) Mask distinguishing stripe and triangular domains based on the triangle GPA magnitudes of sample B shown in Fig. 6. Stripe domains are shown in orange and triangles are shown in blue. (b) Extracted strain for both types of domains in sample B for the same region. Boundary between the different domains is indicated with white lines. (c) Histogram of extracted strain values for both phases.

sample B, we use a threshold on the red and blue triangular domains, as the green GPA amplitude is dominated by the substrate steps, resulting in the mask shown in Fig. 7(a), with 45% of the characterized area triangular phase and 55% stripe phase. The stripe phase is subdivided over the directions in 48% red (parallel to the step edges), 6% green, and less than 1% blue, i.e., 88% of the stripe domains is roughly parallel to the step edges.

For both the stripe domains and the triangular domains, we compute a local periodicity from the gradient of the GPA phases. We then convert this local periodicity to local relative lattice mismatch between the layers $\tilde{\epsilon}$, which is shown in Figs. 7(b) and 7(c). Here, we have taken an average over the three directions for the triangular phase. In total, we observe values of $\tilde{\epsilon}$ between 0.2% and 0.7%. On average, the stripe domains exhibit higher strain values than the triangular domains. Nevertheless, there is a large overlap and additionally a large part of the triangular domains exhibit a mismatch larger than the critical value ϵ_{c1}.

For samples A and C, the triangular domains were not regular enough to obtain a GPA signal. Nevertheless, the GPA amplitudes of the stripe domains indicate the stripe domains well. Therefore, as an alternative approach, masks are created by using a threshold value on these stripe domain amplitudes. Contrary to sample B, for sample A the three different stripe domains are almost divided equally, making up 18%, 17%, and 19% of the area, respectively, for a total of 53% (discrepancy due to rounding) stripe domains and 47% otherwise. Sample C is in between, with stripe domains making up 40%, 11%, and 10%, respectively, for 61% stripe domains in total. Here, like in sample B, the majority stripe direction (in red) is roughly parallel to the step edges.

In Figs. 8 and 9, the occurrence of the three orientations of stripe domains and the extracted relative strain for these samples are shown. Notably, the extracted strain values for the three different samples cover different ranges, with the strain in the stripe domains in sample C significantly lower than in the others.

B. Discussion of extracted strain

Even allowing for error in the extraction of the strain, it is clear that a significant spread of the strain within a phase and a difference between the average strain value for the two phases exists. Furthermore, triangular domains occur at much higher relative lattice mismatch, i.e., the triangles are much smaller than predicted by the Frenkel-Kontorova model. This should be attributed to the modification of the properties of the buffer layer due to its binding to the SiC substrate.

To interpret the stripe domains in terms of strain of the graphene, we need to closely consider what happens in such a

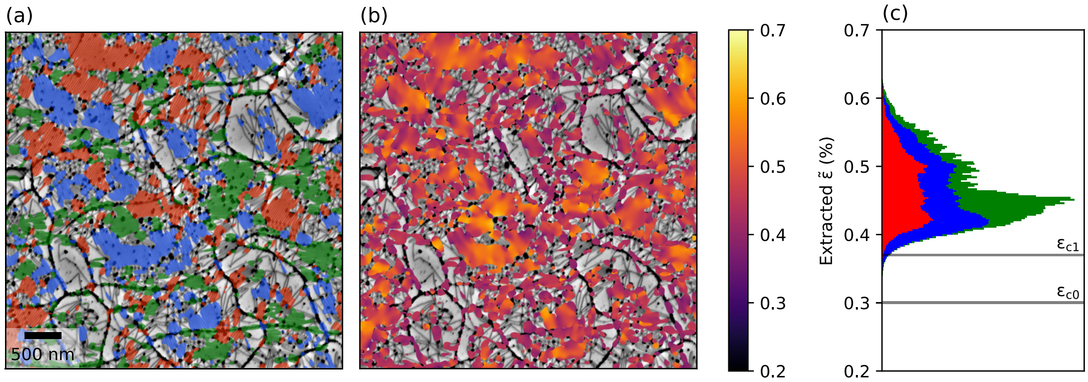

FIG. 8. (a) Mask on sample A based on the GPA amplitudes labeling stripe domains in three directions in red, green, and blue, showing stripe domains of several-hundred-nanometer across. (b) Extracted strain for all three directions of stripe domains for a region in sample A. (c) Histogram of extracted strain values for the three stripe domain directions.

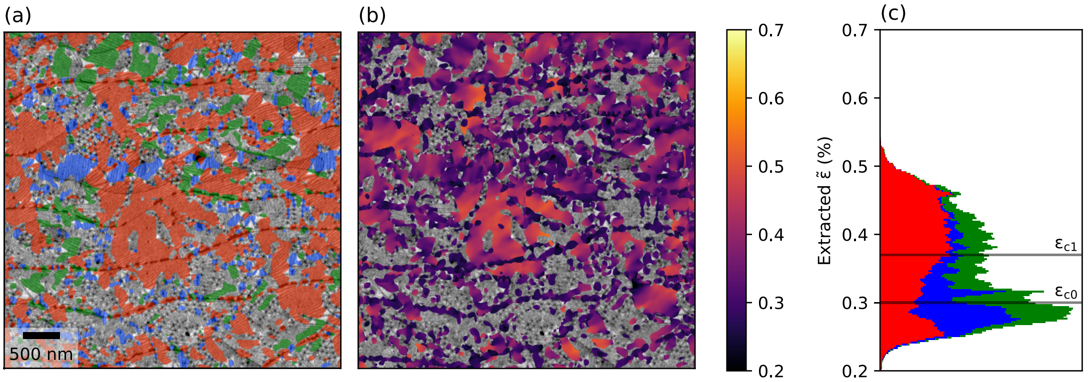

FIG. 9. (a) Mask on sample C based on the GPA amplitudes labeling stripe domain in three directions in red, green, and blue. (b) Extracted strain for all three directions of stripe domains for a region in sample C. (c) Histogram of extracted strain values for the three stripe domain directions.

stripe domain. Perpendicular to the stripe, the average lattice mismatch (at growth temperature) is modified only slightly, like in the 1D FK model. However, parallel to the stripe, the lattice mismatch vanishes as the graphene is strained in that direction to be commensurate to the buffer layer. The variation in stripe period, corresponding to the average lattice mismatch perpendicular to the stripe, is therefore also a measure of the variation and magnitude of the strain itself parallel to the stripe.

Of course, the patches of anisotropic strain in different directions fit together, meaning that there will be local variation in the magnitude and direction of the strain, both relative to the substrate and in absolute terms.

The magnitude of the lattice mismatch and the corresponding size of the domain boundaries explains why epitaxial graphene on SiC exhibits perfect alignment in Low-Energy Electron Diffraction (LEED) experiments. The very fact that the domains are so large that they are visible in LEEM means they are very hard to observe in LEED. A lattice mismatch of 0.7% is too small to derive from the displacement of the first-order graphene spots in a LEEM instrument. Although moiré spots or stripes should, in principle, occur around the (0,0) spot, they tend to be low intensity in bilayer graphene and closer to the (0,0) spot in k space than the typical incident angle spread, even in a well-aligned LEEM instrument.

Furthermore, the variety of domains makes observation in dedicated LEED, or even Spot-Profile Analysis LEED instruments (which could obtain better k-space resolution) impossible, as they lack real-space imaging and the size of the probe is larger than the typical area of similar domains.

For sample B, domain walls in the stripe phases align with one of the domain-wall directions in the triangular phase, i.e., the peaks in the FFT in Fig. 5(c) for both phases are in the same direction. This is in contradiction to the theory of a strained lattice, where the domain walls in the triangular phase run along the zigzag directions of the graphene lattice and the domain walls in the stripe phases along one of the armchair directions [39]. Although the triangular domains in sample A and sample C are not ordered enough to show up as sharp peaks in the FFT, visual inspection of the images indicates a better adherence to this theoretical prediction, but also a spread of the orientation of the triangular domains, which will be explored in more detail in the next section. This does, however, suggest that the step edges in sample B have a strong influence on the direction of the domain boundary, presumably by uniaxially straining the lattice.

IV. SYMMETRY-BREAKING AA SITES (SPIRAL DOMAIN WALLS)

We take a closer look at triangular domains in the different samples in Fig. 10. For these triangular domains, domain boundaries cross in nodes with six connecting domain walls, where the center of the node corresponds to AA stacking; therefore, the nodes are labeled “AA sites.” Taking a closer look at the AA sites, which appear as dark spots in Fig. 10, we observe spiral domain walls. As the six domain boundaries approach an AA site, they do not connect straight to it, but bend, either all to the left or all to the right, before connecting in a small spiral. Such spiral domain boundaries have been observed before in various systems, including epitaxial metal systems such as Cu(111)/Ni(111) and Cu/Ru(1000) interfaces, graphene grown on copper, and 2H-1T polytype heterostructures in TaS_2 [16,33,44–47], and have been reproduced in simulations [48,49].

A tentative intuitive explanation for the occurrence of these spiral domain walls is that they are a result of the shear domain boundary having lower energy cost per unit length than the strain-type domain boundary. Thus a deviation from straight

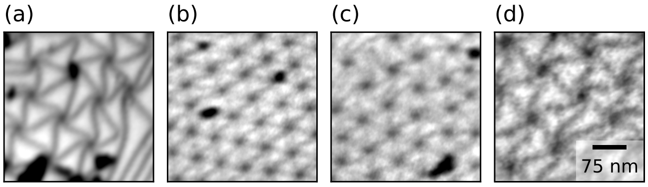

FIG. 10. (a) Spiral domain walls around AA sites in sample A. (b) Very regular triangles with very little spiral rotation in sample B. (c) Less regular area of sample B with more rotation in each spiral and opposing orientations. (d) Spiral domain walls in sample C. Contrast optimized per sample; scale bar valid for all images in this figure.

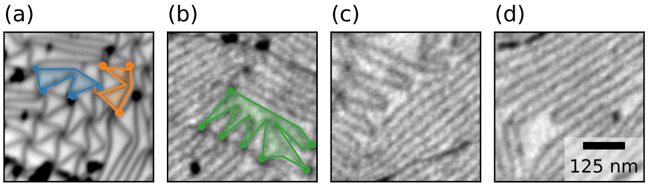

FIG. 11. (a) Detail of sample A. Two sets of four AA nodes, each set bordering one domain, are indicated in blue and orange. Each of these domains therefore contains one edge dislocation. (b) Detail of sample C. A set of seven AA nodes bordering a single domain is indicated in green. This domain therefore contains multiple edge dislocations. Each edge dislocation also corresponds to a domain boundary with a characteristic kink in it, forming a triangle with another domain boundary connecting the same nodes. (c),(d) Details of sample C showing more kinked domain boundaries at the edges of the striped domain areas. Contrast optimized per sample; scale bar valid for all images in this figure.

domain boundaries is promoted in the case of strain domain boundaries, but no such deviation is forced in the case of pure twist, where the domain boundaries are already in the lowest possible energy configuration [39].

In the samples studied here, both orientations of spirals occur, even on the same SiC terrace, even as direct neighbors. According to simulations of a wide variety of twist angles, biaxial strain, and combinations thereof [49], a coexistence of both spiral orientations is an indication of pure lattice mismatch, without twist angle (as we would expect for this system), as the system is mirror symmetric and only the spiral itself breaks the symmetry. A pure twist moiré pattern would be signaled by no spiraling and, indeed, no spiraling is visible in twisted bilayer graphene (TBG) samples [20,22,50]. For a combination of strain and a small twist between the layers, the mirror symmetry is broken and all spirals should align.

There is variation in how much the spirals curl near the AA sites. It seems to depend on the sample, but there is even variation on the same sample, as exemplified by the difference between Figs. 10(b) and 10(c), both on sample B. Curiously, the moiré lattice also seems somewhat rotated between Figs. 10(b) and 10(c), indicating that in at least one of the two cases a local twist between the graphene and buffer layer occurs in addition to the biaxial strain. A biaxial strain magnifies the relative twist of the atomic lattices, similar to how a twist angle magnifies a uniaxial strain. In this case, the atomic twist angle θ_a can be expressed as a function of the biaxial strain ϵ and the apparent moiré twist angle θ as follows [51]:

$$\theta_a = \theta - \arcsin\left(\frac{\sin\theta}{1+\epsilon}\right) \approx \epsilon\theta.$$

Therefore, the observed moiré angle difference of the moiré patterns in Figs. 10(b) and 10(c) of $\theta \approx 15^\circ$ at a strain of $\epsilon \approx 0.45\%$ corresponds to a twist angle difference of the atomic lattices of $\theta_a \approx 0.07^\circ$. Here, the lattice in Fig. 10(b) should actually correspond to a larger twist than the one in Fig. 10(c). Note that this twist angle is the average angle between the unrelaxed lattices, as the atomic lattices within the domain are commensurate.

To fully analyze this, an optimization approach disentangling strain and twist just like employed for the case of twisted bilayer graphene could be used [22,52].

Nevertheless, this demonstrates that the triangular moiré pattern is not only a very sensitive measure of the lattice constant mismatch, but in the presence of such a lattice constant mismatch, the direction of the spiraling of the domain boundaries combined with the orientation of the moiré lattice is a very sensitive probe to the relative local orientation.

V. TOPOLOGICAL DEFECTS: EDGE DISLOCATIONS

The strain-caused moiré patterns observed in these systems magnify topological defects of the atomic lattice, just like in the twisted bilayer graphene case [22]. A particular example of such topological defects is an edge dislocation, where a half row of unit cells is added in a graphene layer, distorting the atom positions around the end of the half row, where a 5-ring/7-ring defect forms. These edge dislocations cause intervalley scattering of the electrons in bilayer graphene on SiC [14]. In the absence of any edge dislocations in the graphene layer and the buffer layer, each domain borders on precisely three AA nodes and each pair of neighboring AA nodes has only one domain boundary connecting them. Therefore, any deviation from these two rules indicates an atomic edge dislocation in one of the constituting layers.

Despite the fact that we can expect the number of edge dislocations in the underlying SiC substrate, and therefore in the buffer layer, to be very low on these microscopic levels [53,54], we observe many such defects in all three samples, although in different densities. Examples for sample A and sample C are shown in Fig. 11. Contrary to the TBG case, domain boundaries near edge dislocations in areas with more disorder deform the surrounding lattice significantly, with a domain boundary crossing over to the next domain boundary often with a significant kink, i.e., domain boundaries running between the same nodes repel each other and form a triangle. Earlier imaging experiments have shown that the atomic dislocations themselves are located in the kink [14,55].

Edge dislocations in highly ordered areas in sample B, both in triangular and stripe areas, show minimal distortion of the surrounding lattice. Using GPA, we can highlight these atomic edge dislocations, just like in TBG, as shown in Fig. 12, except in the case when the Burgers vector corresponding to the dislocation is parallel to the stripes (as is the case for the dislocation indicated with the orange circle).

As the density of dislocations is not dominated by edge dislocations in the buffer-layer/SiC substrate itself, this should be another indicator of the quality of the graphene layer. In particular in sample C, high numbers of dislocations within a single stacking domain are found between areas of different stripe directions. This suggests that stripe domains might already form during growth, with three different stripe directions and therefore different strain directions, as well as a mismatch of their lattice vectors due to this. As they continue to grow and coalesce, this lattice mismatch can only be reconciled with edge dislocations, reminiscent of the rotational domain boundaries in graphene grown by chemical vapor deposition (CVD). However, in this case, the atomic lattice in the

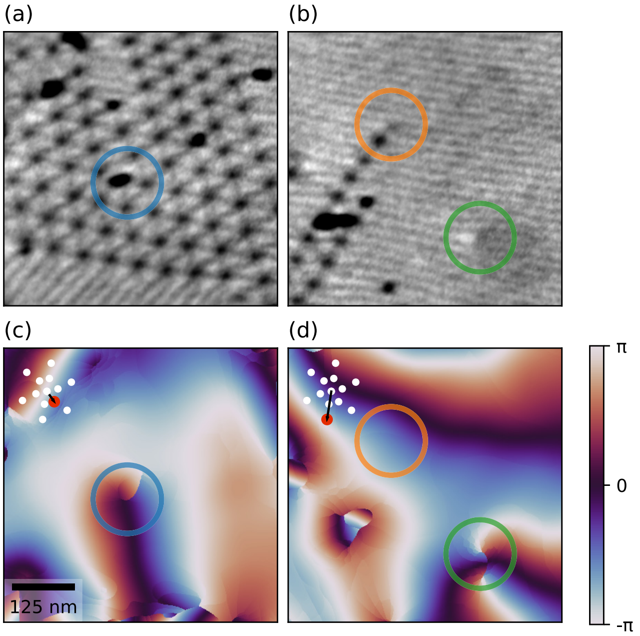

FIG. 12. Dislocations in sample B. (a) Dislocation in a triangular domain area at the center of the blue circle. (b) Two dislocations in a stripe domain area, indicated by orange and green circles. (c) GPA phases of (a), where the dislocation corresponds to a singularity in the GPA phase. (d) Similarly, GPA phase for the stripe domain in (b). The singularity of the dislocation in the lower right is of the order of 2, as the Burgers vector is parallel to the lattice vector corresponding to the GPA phase. The singularity at the end of the AA-node chain in the upper left is not visible in the GPA phase, as the Burgers vector is perpendicular to the relevant lattice vector. Insets of (c) and (d) indicate the corresponding reciprocal vectors of the GPA phases. The scale bar in (c) applies to all panels.

different domains is oriented the same, but slightly elongated in different directions. Therefore, the mismatch between the average lattice vectors is much smaller and the density of edge dislocations along such a boundary is much lower.

VI. CONCLUSION AND OUTLOOK

In this work, we have shown that LEEM imaging of domain boundaries in epitaxial graphene on SiC enables the study of strain and atomic edge dislocations on large scales. We found that the growth conditions of high-quality graphene on SiC cause areas of anisotropic stripes in different directions. We have shown that these stripe domains might already form during the nucleation phase of the growth (as opposed to during cool down) and cause atomic edge dislocations when different directions grow together.

The growth temperature, growth duration, and the amount of carbon that is predeposited all have significant effects on the growth, but also on the domain boundaries that are formed. A combination of triangular and stripe domains between a buffer layer and the lowest graphene layer are universally occurring for all studied samples, indicating that all samples are close to the phase transition between the two types of domains. Nevertheless, the density of the domain boundaries, the ratio between the triangular and stripe domains, and the density of edge dislocations vary according to sample type and growth conditions. Thus the study of these domain boundaries can aid the optimization of growth parameters. In addition to these known parameters influencing the growth, we have seen strong indications that the direction of the step edges of the substrate with respect to the atomic lattice influences the stacking domains and the directions of the domain boundaries with respect to the atomic lattice. Therefore, this miscut direction also influences the quality of the resulting graphene. Finally, similar to the TBG case, we expect that the topological defects in the domain boundary network can be interesting in itself, e.g., for their local electronic properties.

In this work, we have only scratched the surface of the information available in these domain boundary datasets. Therefore, the data has been made available in Ref. [26]. Furthermore, here we give a few more suggestions of information that could be extracted, but are beyond the scope of this work. First, it would be informative to connect the images directly to the atomic lattice directions, either by connecting to LEED data or possibly by observing the local directions of the substrate step edges. Second, for the triangular domains, the local uniaxial strain, biaxial strain, and twist should be separated using a Kerelsky-style decomposition based on the extracted k vectors as described for the TBG case in Refs. [22,52]. Third, statistics of left versus right orientation spiral domain walls as a function of the local (minimal) twist angle between the lattices could be obtained. These could be used to measure energy differences as a function of twist angle and strain. Finally, it would be worthwhile to use AC-LEEM to observe the dynamics of domain walls, to study the stability of the orientation of spiral domain walls in the twist-free case, and potentially obtain more detailed experimental data on the energy landscape that governs these domain boundaries.

ACKNOWLEDGMENTS

We thank Marcel Hesselberth and Douwe Scholma for their indispensable technical support. We thank Christian Ott, Heiko Weber, Davood Momeni, and Klaus Pierz for graphene supply and Robbert Schoo, Cees Flipse, Anna Sinterhauf, and Martin Wenderoth for sharing their samples. This work was supported by the Netherlands Organisation for Scientific Research (NWO/OCW) as part of the Frontiers of Nanoscience program.

[1] A. J. Van Bommel, J. E. Crombeen, and A. Van Tooren, LEED and Auger electron observations of the SiC(0001) surface, Surf. Sci. **48**, 463 (1975).

[2] C. Riedl, U. Starke, J. Bernhardt, M. Franke, and K. Heinz, Structural properties of the graphene-SiC(0001) interface as a key for the preparation of homogeneous

large-terrace graphene surfaces, Phys. Rev. B **76**, 245406 (2007).

[3] C. Riedl, C. Coletti, T. Iwasaki, A. A. Zakharov, and U. Starke, Quasi-Free-Standing Epitaxial Graphene on SiC Obtained by Hydrogen Intercalation, Phys. Rev. Lett. **103**, 246804 (2009).

[4] S. Goler, C. Coletti, V. Piazza, P. Pingue, F. Colangelo, V. Pellegrini, K. V. Emtsev, S. Forti, U. Starke, F. Beltram, and S. Heun, Revealing the atomic structure of the buffer layer between SiC(0 0 0 1) and epitaxial graphene, Carbon **51**, 249 (2013).

[5] S. Tanaka, K. Morita, and H. Hibino, Anisotropic layer-by-layer growth of graphene on vicinal SiC(0001) surfaces, Phys. Rev. B **81**, 041406(R) (2010).

[6] J. B. Hannon, M. Copel, and R. M. Tromp, Direct Measurement of the Growth Mode of Graphene on SiC(0001) and SiC(000$\bar{1}$), Phys. Rev. Lett. **107**, 166101 (2011).

[7] R. M. Tromp and J. B. Hannon, Thermodynamics and Kinetics of Graphene Growth on SiC(0001), Phys. Rev. Lett. **102**, 106104 (2009).

[8] K. V. Emtsev, A. Bostwick, K. Horn, J. Jobst, G. L. Kellogg, L. Ley, J. L. McChesney, T. Ohta, S. A. Reshanov, J. Röhrl, E. Rotenberg, A. K. Schmid, D. Waldmann, H. B. Weber, and T. Seyller, Towards wafer-size graphene layers by atmospheric pressure graphitization of silicon carbide, Nat. Mater. **8**, 203 (2009).

[9] M. Kruskopf, D. M. Pakdehi, K. Pierz, S. Wundrack, R. Stosch, T. Dziomba, M. Götz, J. Baringhaus, J. Aprojanz, C. Tegenkamp, J. Lidzba, T. Seyller, F. Hohls, F. J. Ahlers, and H. W. Schumacher, Comeback of epitaxial graphene for electronics: Large-area growth of bilayer-free graphene on SiC, 2D Mater. **3**, 041002 (2016).

[10] D. Momeni Pakdehi, J. Aprojanz, A. Sinterhauf, K. Pierz, M. Kruskopf, P. Willke, J. Baringhaus, J. P. Stöckmann, G. A. Traeger, F. Hohls, C. Tegenkamp, M. Wenderoth, F. J. Ahlers, and H. W. Schumacher, Minimum resistance anisotropy of epitaxial graphene on SiC, ACS Appl. Mater. Interfaces **10**, 6039 (2018).

[11] S. Sonde, F. Giannazzo, C. Vecchio, R. Yakimova, E. Rimini, and V. Raineri, Role of graphene/substrate interface on the local transport properties of the two-dimensional electron gas, Appl. Phys. Lett. **97**, 132101 (2010).

[12] S. Kim, J. Ihm, H. J. Choi, and Y.-W. Son, Origin of Anomalous Electronic Structures of Epitaxial Graphene on Silicon Carbide, Phys. Rev. Lett. **100**, 176802 (2008).

[13] T. A. de Jong, E. E. Krasovskii, C. Ott, R. M. Tromp, S. J. van der Molen, and J. Jobst, Intrinsic stacking domains in graphene on silicon carbide: A pathway for intercalation, Phys. Rev. Mater. **2**, 104005 (2018).

[14] S. Cho, S. D. Kang, W. Kim, E.-S. Lee, S.-J. Woo, K.-J. Kong, I. Kim, H.-D. Kim, T. Zhang, J. A. Stroscio, Y.-H. Kim, and H.-K. Lyeo, Thermoelectric imaging of structural disorder in epitaxial graphene, Nat. Mater. **12**, 913 (2013).

[15] H. Hibino, S. Mizuno, H. Kageshima, M. Nagase, and H. Yamaguchi, Stacking domains of epitaxial few-layer graphene on SiC(0001), Phys. Rev. B **80**, 085406 (2009).

[16] B. Lalmi, J. C. Girard, E. Pallecchi, M. Silly, C. David, S. Latil, F. Sirotti, and A. Ouerghi, Flower-Shaped Domains and Wrinkles in Trilayer Epitaxial Graphene on Silicon Carbide, Sci. Rep. **4**, 4066 (2014).

[17] I. Martin, Y. M. Blanter, and A. F. Morpurgo, Topological Confinement in Bilayer Graphene, Phys. Rev. Lett. **100**, 036804 (2008).

[18] L. Ju Jr, Z. Shi, N. Nair, Y. Lv, C. Jin, J. Velasco, C. Ojeda-Aristizabal, H. A. Bechtel, M. C. Martin, A. Zettl, J. Analytis, and F. Wang, Topological valley transport at bilayer graphene domain walls, Nature (London) **520**, 650 (2015).

[19] S. Huang, K. Kim, D. K. Efimkin, T. Lovorn, T. Taniguchi, K. Watanabe, A. H. MacDonald, E. Tutuc, and B. J. LeRoy, Topologically Protected Helical States in Minimally Twisted Bilayer Graphene, Phys. Rev. Lett. **121**, 037702 (2018).

[20] J. D. Verbakel, Q. Yao, K. Sotthewes, and H. J. W. Zandvliet, Valley-protected one-dimensional states in small-angle twisted bilayer graphene, Phys. Rev. B **103**, 165134 (2021).

[21] T. A. de Jong, X. Chen, J. Jobst, E. E. Krasovskii, R. M. Tromp, and S. J. van der Molen, Low-energy electron microscopy contrast of stacking boundaries: Comparing twisted few-layer graphene and strained epitaxial graphene on silicon carbide, Phys. Rev. B **107**, 075431 (2023).

[22] T. A. de Jong, T. Benschop, X. Chen, E. E. Krasovskii, M. J. A. de Dood, R. M. Tromp, M. P. Allan, and S. J. van der Molen, Imaging moiré deformation and dynamics in twisted bilayer graphene, Nat. Commun. **13**, 70 (2022).

[23] C. Ott, Light and electron emission at epitaxial graphene nano-contacts, Ph.D. thesis, Friedrich-Alexander-Universität Erlangen-Nürnberg, 2021, https://opus4.kobv.de/opus4-fau/files/16722/ChristianOttDissertation.pdf.

[24] G. R. Yazdi, R. Vasiliauskas, T. Iakimov, A. Zakharov, M. Syväjärvi, and R. Yakimova, Growth of large area monolayer graphene on 3C-SiC and a comparison with other SiC polytypes, Carbon **57**, 477 (2013).

[25] T. A. de Jong, Graphene stacking domains code, Code repository on ZENODO, https://doi.org//10.5281/zenodo.7554283.

[26] T. A. de Jong, J. Jobst, and S. J. van der Molen, Data underlying the paper: Stacking domain morphology in epitaxial graphene on silicon carbide., Dataset on 4TU.ResearchData, https://doi.org/10.4121/21930768.

[27] D. Momeni Pakdehi, P. Schädlich, T. T. N. Nguyen, A. A. Zakharov, S. Wundrack, E. Najafidehaghani, F. Speck, K. Pierz, T. Seyller, C. Tegenkamp, and H. W. Schumacher, Silicon carbide stacking-order-induced doping variation in epitaxial graphene, Adv. Funct. Mater. **30**, 2004695 (2020).

[28] A. Sinterhauf, G. A. Traeger, D. Momeni Pakdehi, P. Schädlich, P. Willke, F. Speck, T. Seyller, C. Tegenkamp, K. Pierz, H. W. Schumacher, and M. Wenderoth, Substrate induced nanoscale resistance variation in epitaxial graphene, Nat. Commun. **11**, 555 (2020).

[29] F. Speck, M. Ostler, S. Besendörfer, J. Krone, M. Wanke, and T. Seyller, Growth and intercalation of graphene on silicon carbide studied by low-energy electron microscopy, Annal. Phys. **529**, 1700046 (2017).

[30] B. Butz, C. Dolle, F. Niekiel, K. Weber, D. Waldmann, H. B. Weber, B. Meyer, and E. Spiecker, Dislocations in bilayer graphene, Nature (London) **505**, 533 (2014).

[31] D. Halbertal, N. R. Finney, S. S. Sunku, A. Kerelsky, C. Rubio-Verdú, S. Shabani, L. Xian, S. Carr, S. Chen, C. Zhang, L. Wang, D. Gonzalez-Acevedo, A. S. McLeod, D. Rhodes, K. Watanabe, T. Taniguchi, E. Kaxiras, C. R. Dean, J. C. Hone, A. N. Pasupathy *et al.*, Moiré metrology of energy landscapes in van der Waals heterostructures, Nat. Commun. **12**, 242 (2021).

[32] R. Guerrero-Avilés, M. Pelc, F. R. Geisenhof, R. T. Weitz, and A. Ayuela, Rhombohedral trilayer graphene is more stable than its Bernal counterpart, Nanoscale **14**, 16295 (2022).

[33] J. Ravnik, I. Vaskivskyi, Y. Gerasimenko, M. Diego, J. Vodeb, V. Kabanov, and D. D. Mihailovic, Strain-induced metastable topological networks in laser-fabricated TaS_2 polytype heterostructures for nanoscale devices, ACS Appl. Nano Mater. **2**, 3743 (2019).

[34] D. A. Schmidt, T. Ohta, and T. E. Beechem, Strain and charge carrier coupling in epitaxial graphene, Phys. Rev. B **84**, 235422 (2011).

[35] T. Schumann, M. Dubslaff, M. H. Oliveira, M. Hanke, J. M. J. Lopes, and H. Riechert, Effect of buffer layer coupling on the lattice parameter of epitaxial graphene on SiC(0001), Phys. Rev. B **90**, 041403(R) (2014).

[36] N. Ferralis, R. Maboudian, and C. Carraro, Evidence of Structural Strain in Epitaxial Graphene Layers on 6H-SiC(0001), Phys. Rev. Lett. **101**, 156801 (2008).

[37] J. Bao, W. Norimatsu, H. Iwata, K. Matsuda, T. Ito, and M. Kusunoki, Synthesis of Freestanding Graphene on SiC by a Rapid-Cooling Technique, Phys. Rev. Lett. **117**, 205501 (2016).

[38] N. Ferralis, J. Kawasaki, R. Maboudian, and C. Carraro, Evolution in surface morphology of epitaxial graphene layers on SiC induced by controlled structural strain, Appl. Phys. Lett. **93**, 191916 (2008).

[39] I. V. Lebedeva and A. M. Popov, Two Phases with Different Domain Wall Networks and a Reentrant Phase Transition in Bilayer Graphene under Strain, Phys. Rev. Lett. **124**, 116101 (2020).

[40] J. S. Alden, A. W. Tsen, P. Y. Huang, R. Hovden, L. Brown, J. Park, D. A. Muller, and P. L. McEuen, Strain solitons and topological defects in bilayer graphene, Proc. Natl. Acad. Sci. **110**, 11256 (2013).

[41] H. Hattab, A. T. N'Diaye, D. Wall, C. Klein, G. Jnawali, J. Coraux, C. Busse, R. van Gastel, B. Poelsema, T. Michely, F.-J. Meyer zu Heringdorf, and M. Horn-von Hoegen, Interplay of wrinkles, strain, and lattice parameter in graphene on iridium, Nano Lett. **12**, 678 (2012).

[42] P. Sutter, J. T. Sadowski, and E. Sutter, Graphene on Pt(111): Growth and substrate interaction, Phys. Rev. B **80**, 245411 (2009).

[43] T. Benschop, T. A. de Jong, P. Stepanov, X. Lu, V. Stalman, S. J. van der Molen, D. K. Efetov, and M. P. Allan, Measuring local moiré lattice heterogeneity of twisted bilayer graphene, Phys. Rev. Res. **3**, 013153 (2021).

[44] C. Gutiérrez, C.-J. Kim, L. Brown, T. Schiros, D. Nordlund, E. B. Lochocki, K. M. Shen, J. Park, and A. N. Pasupathy, Imaging chiral symmetry breaking from Kekulé bond order in graphene, Nat. Phys. **12**, 950 (2016).

[45] S. Shao, J. Wang, A. Misra, and R. G. Hoagland, Spiral patterns of dislocations at nodes in (111) semi-coherent FCC interfaces, Sci. Rep. **3**, 2448 (2013).

[46] J. C. Hamilton and S. M. Foiles, Misfit Dislocation Structure for Close-Packed Metal-Metal Interfaces, Phys. Rev. Lett. **75**, 882 (1995).

[47] C. Günther, J. Vrijmoeth, R. Q. Hwang, and R. J. Behm, Strain Relaxation in Hexagonally Close-Packed Metal-Metal Interfaces, Phys. Rev. Lett. **74**, 754 (1995).

[48] J. A. Snyman and H. C. Snyman, Computed epitaxial monolayer structures: III. Two-dimensional model: zero average strain monolayer structures in the case of hexagonal interfacial symmetry, Surf. Sci. **105**, 357 (1981).

[49] S. Quan, L. He, and Y. Ni, Tunable mosaic structures in van der Waals layered materials, Phys. Chem. Chem. Phys. **20**, 25428 (2018).

[50] H. Yoo, R. Engelke, S. Carr, S. Fang, K. Zhang, P. Cazeaux, S. H. Sung, R. Hovden, A. W. Tsen, T. Taniguchi, K. Watanabe, G.-C. Yi, M. Kim, M. Luskin, E. B. Tadmor, E. Kaxiras, and P. Kim, Atomic and electronic reconstruction at the van der Waals interface in twisted bilayer graphene, Nat. Mater. **18**, 448 (2019).

[51] For any realistic atomic strain, this expression is valid for $|\theta_a| \lesssim \epsilon$, but the crossover at $\theta = 30^\circ$ makes it impossible to distinguish the sign for $|\theta_a| \gtrsim \frac{\epsilon}{2}$ in BF-LEEM.

[52] A. Kerelsky, L. J. McGilly, D. M. Kennes, L. Xian, M. Yankowitz, S. Chen, K. Watanabe, T. Taniguchi, J. Hone, C. Dean, A. Rubio, and A. N. Pasupathy, Maximized electron interactions at the magic angle in twisted bilayer graphene, Nature (London) **572**, 95 (2019).

[53] T. Kimoto and H. Watanabe, Defect engineering in SiC technology for high-voltage power devices, Appl. Phys. Express **13**, 120101 (2020).

[54] J. Łażewski, P. T. Jochym, P. Piekarz, M. Sternik, K. Parlinski, J. Cholewiński, P. Dłużewski, and S. Krukowski, DFT modelling of the edge dislocation in 4H-SiC, J. Mater. Sci. **54**, 10737 (2019).

[55] P. Schweizer, C. Dolle, and E. Spiecker, *In situ* manipulation and switching of dislocations in bilayer graphene, Sci. Adv. **4**, eaat4712 (2018).